NUMERICAL HEAT TRANSFER, PART A: APPLICATIONS
2019, VOL. 76, NO. 5, 301–322
https://doi.org/10.1080/10407782.2019.1627829

Numerical analysis of meniscus dynamics in monolayer-wick dropwise condensation

S. Modak[a], M. Kaviany[a], S. Hoenig[b], and R. Bonner[b]

[a]Department of Mechanical Engineering, University of Michigan, Ann Arbor, Michigan, USA; [b]Advanced Cooling Technologies, Inc, Lancaster, Pennsylvania, USA

ABSTRACT

The effect of hydrophobic monolayer sintered-particle wick on the growth and departure of droplets in dropwise condensation over a vertical surface is analyzed numerically using the minimum meniscus surface energy principle and the direct simulation of the meniscus and heat transfer through the partially liquid-filled pores. The condensate fills the pores, increases the capillary pressure, and joins with the menisci from adjacent pores, leading to a droplet formation. The droplet growth is supported by liquid supply from the adjacent pores until the critical droplet departure volume is reached. The heat transfer rate is controlled by the average meniscus thickness, and the droplet surface coverage. Based on these and the plain–surface limit (for very small and very large particle diameter d_p), a threshold band of d_p is predicted below which the dropwise condensation rate is slightly enhanced compared to the plain, hydrophobic surface. The analysis explains the existing experimental results (and new augmented experimental results) and the challenges in further enhancing the dropwise condensation with surface microstructures.

ARTICLE HISTORY
Received 28 February 2019
Accepted 31 May 2019

1. Introduction

Dropwise condensation is manifested by the droplet-size distribution on the surface and the microstructure of the surface. Studies suggest that even though individual droplets experience growth and coalescence, the droplet distribution on a surface can be assumed to be static [1]. Bonner [2] developed droplet distribution correlations using the Le Fevre and Rose framework [3], for water and organic fluids, and examined the effect of the surface inclination with respect to the gravity. The dropwise condensation demonstrates higher heat transfer coefficient compared to filmwise condensation, due to the low thermal resistance of the smaller droplets [4]. Mikic [5] suggests that droplets with diameter > 0.2 mm can be considered as insulators, while the smaller ones can be assumed to be responsible for all the heat transfer though the surface. Laboratory trials have shown that hydrophobic coatings enhance dropwise condensation by reducing the wettability of the surface, however, efforts to develop durable coatings have had limited success [1].

The micro-patterning of the surface affects the surface wettability and the droplet size distribution, demonstrating an important role in enhancing the condensation rate. Enhancements of filmwise and dropwise condensation have been achieved with millimeter vertical grooves or flutes [6,7], and microscale posts and indentations [8]. Monolayer wicks are commonly used to spread the liquid for evaporation [9]. In recent experimental investigation using hydrophobic monolayer

CONTACT M. Kaviany kaviany@umich.edu Department of Mechanical Engineering, University of Michigan, Ann Arbor, MI 48109, USA.
Color versions of one or more of the figures in the article can be found online at www.tandfonline.com/unht.

Nomenclature

A	area (m^2)
AR	area thermal resistance [K/(W/m^2)]
Bo_d	bond number $\Delta\rho_{lg}gd_d^2/\sigma$
c_{flood}	flood regime resistance constant
d	diameter (m)
E	energy (J)
F_e	force vector at the contact line (N)
g	gravitational acceleration vector (m/s^2)
h	heat transfer coefficient (W/m^2-K)
k	thermal conductivity (W/m-K)
l	length along contact line (m)
l_i	half-cell diagonal length (m)
l_k	chord length (m)
p	pressure (Pa)
p_c	capillary pressure (Pa)
q	heat flux vector (W/m^2)
Q	heat flow rate (W)
R	thermal resistance (K/W)
r	radius (m)
s_l	liquid saturation volume fraction
T	temperature (°C, K)
V	volume (m^3)
x	fraction of surface covered by droplets

Greek Symbols

α	meniscus contact line apex angle (°)
β	chord angle (°)
σ	surface tension (N/m)
Σ	overall
θ_c	contact angle (°)
θ_0	particle base azimuthal angle (°)
δ_l	liquid thickness (m)
$\Delta\rho_{lg}$	gas–liquid density difference (kg/m3)

Subscripts

c	condensation or capillary or contact
Cu	copper
d	droplet
d,c	droplet in coverage regime
$d,flood$	droplet in flood regime
$d,pore$	droplet in pore regime
e	evaporation
eq	equilibrium
l,f	liquid film
g	gas
l	liquid
lg	liquid–gas
l-g	liquid vapor interface
m	meniscus
mw	monolayer wick
max	maximum
min	minimum
p	particle
ps	plain surface
I	transition from roughness to wick regime
II	transition from wick to fin regime

wicks [10], it is shown that a monolayer (sintered copper particles) can enhance the dropwise condensation (compared to the plain surface) when the particle diameter is smaller than 10 μm, while larger particles decrease the heat transfer coefficient. In a monolayer wick, the condensate forms a meniscus within the pores and condensation occurs at the surface of the meniscus as well as on the particle surface above the meniscus, as rendered in Figure 1. The condensation at the meniscus causes it to rise and fill the pores between the particles, and then coalesce with the neighboring menisci to form droplets.

Droplets grow either by coalescing and receiving condensate from the neighboring menisci or by meniscus thickness growth through the pore. The meniscus thickness is an important contributor to the thermal resistance of the wick and depends on the contact angle and the particle diameter. Condensation occurring on the particle surface (protruding from the meniscus) depends on the particle diameter, and contributes more when the particle are large (as the particle diameter increases, the meniscus thickness increases and the meniscus thermal conduction resistance becomes comparable to that through the particle). Here, we analyze and model these combined mechanisms of condensation. We expand on the bimodal size distribution model of [5], where the smaller droplets ($d_d < 0.2$ mm) are further divided into two modes and are responsible for the heat transfer through the larger droplets ($d_d > 0.2$ mm) (covering area fraction x) is neglected and is assumed to occur through surface area fraction $1 - x$ (occupied by droplets with $d_d < 0.2$ mm). We use the principles of minimum meniscus energy (numerically solved) for the topology of the growing condensate in the monolayer wick pores (Section 2). Section 3 uses direct numerical heat transfer simulations to analyze the role of the sintered particle diameter on the condensation enhancement (compared to the plain surface). Section 4 compares these predictions with the experimental results of [10] and the newly obtained experimental results reported here for large particle diameters (Appendix A).

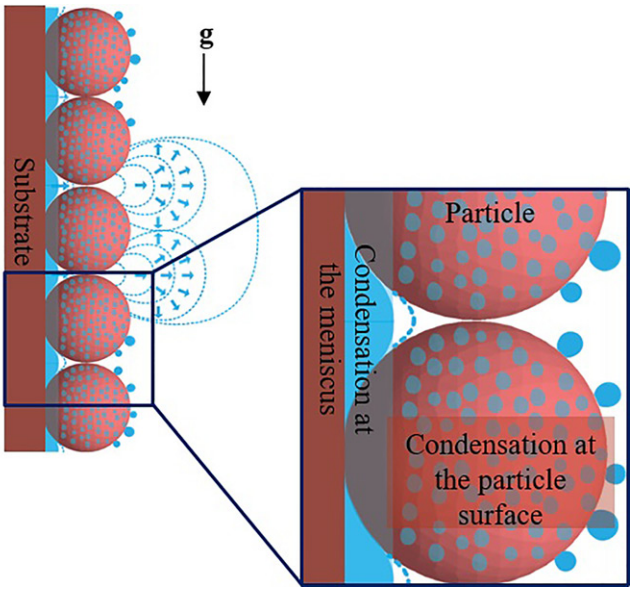

Figure 1. Rendering of the dropwise condensation on the sintered-particle monolayer wick over a vertical plate showing condensate growth by condensation at the meniscus surface and on the particles.

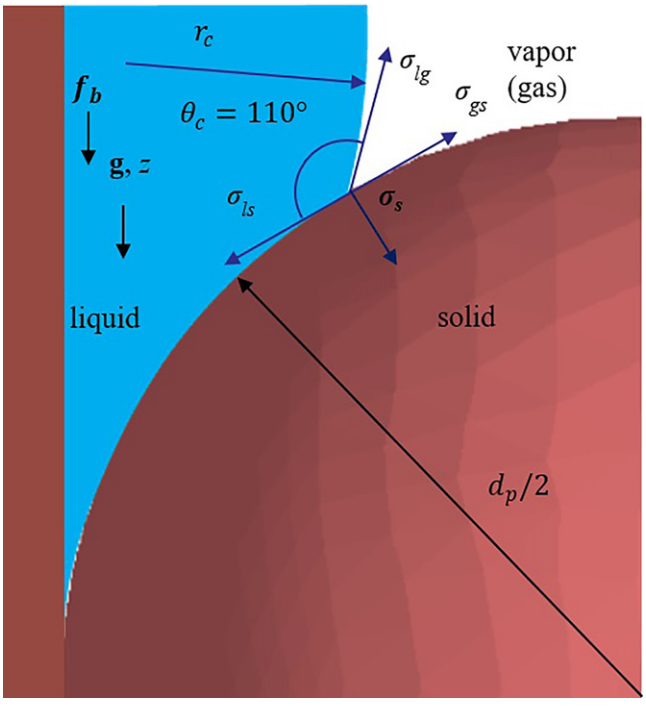

Figure 2. The interfacial tensions and gravity force acting on the meniscus and the liquid volume. The contact line and angle are shown in this two-dimensional rendering.

2. Numerical analysis of meniscus dynamics in the monolayer wick

The dynamical transitions of the meniscus considers the body and surface forces acting on it, as shown in Figure 2. These interfacial tension forces determine the contact angle θ_c and the average meniscus radius of curvature r_c, which in turn controls the capillary pressure [11]

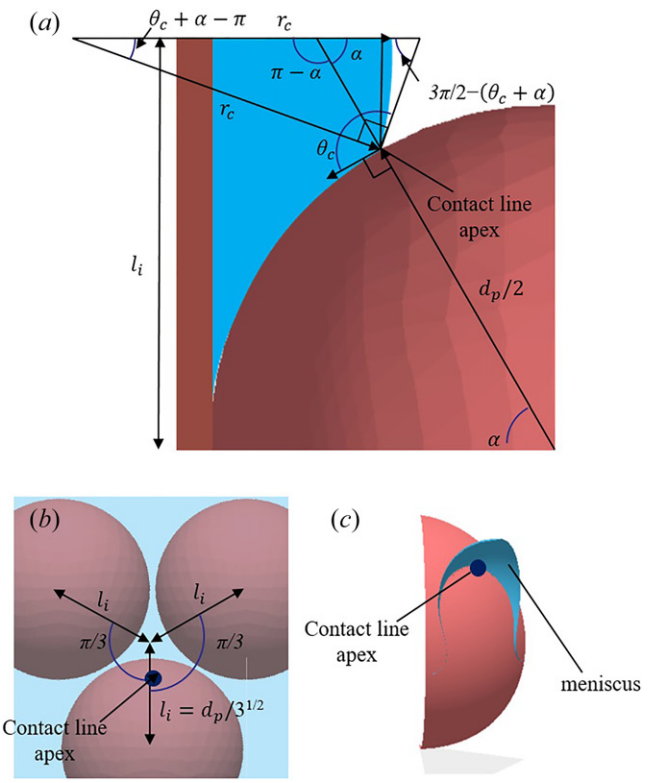

Figure 3. (*a*) Determination of r_c and l_i using the trigonometric relations based on α and θ_c. (*b*) Top view of hexagonal packing (HCP) array showing d_i and the contact-line apex. (*c*) Oblique view snapshot of the Surface Evolver simulation cell showing the contact-line apex for which α is calculated.

$$p_c = p_l - p_g = 2\sigma_{lg}\cos\theta_c/r_c, \tag{1}$$

$$1/r_c = 1/r_1 + 1/r_2, \tag{2}$$

where r_1 and r_2 are the principal radii of curvature and

$$\cos\theta_c = (\sigma_{sg} - \sigma_{ls})/\sigma_{lg}. \tag{3}$$

The capillary pressure and the contact angle primarily determine the meniscus topology, while the effect of a body force such as the gravity are negligible for small Bond numbers. The analytical estimate of the Leverett and Melrose function for the capillary pressure includes the effects of the permeability and wettability (contact angle) [12,13] for the bulk, partially liquid saturated porous media. Here an analytical relation is developed for the capillary pressure based on the results of numerical simulations with the software Surface Evolver [14].

2.1. Capillary pressure

The capillary pressure is estimated analytically along the meniscus contact line using the half-cell length l_i and the contact-line apex angle α, as shown in Figure 3*a*. The dimensionless capillary pressure p_c^* is

$$p_c^* = -p_c d_p/(\sigma_{lg}\cos\theta_c). \tag{4}$$

This is similar to the Leverett function [12,15], except here d_p is used as the length scale. The radius curvature r_c, using the trigonometric relations shown in Figures 3*a* and 3*b*, is

$$r_c = \left\{\left[(\sin\alpha)d_p/2\right] - l_i\right\}/\sin(\theta_c + \alpha). \tag{5}$$

Using Eqs. (1, 4, 5), we have

$$p_c^* = 4\sin(\theta_c + \alpha)/\left(\sin\alpha - 2l_i/d_p\right). \tag{6}$$

The maximum pressure $p^*_{c,max}$ (with respect to α) is found from Eqs. (4–6), and is

$$p^*_{c,max} = 4/\left\{\left[4\left(l_i/d_p\right)^2 - \sin^2\theta_c\right]^{1/2} - |\cos\theta_c\right\}. \tag{7}$$

Substituting $p^*_{c,max}$ from Eq. (7) into Eq. (4) and solving for p_c, we have

$$p_{c,max} = 4\sigma_{lg}\cos\theta_c/\left(d_p\left\{\left|\cos\theta_c - \left[4\left(l_i/d_p\right)^2 - \sin^2\theta_c\right]^{1/2}\right\}\right). \tag{8}$$

Equation (8) gives results close to the $p_{c,max}$ obtained in [9] for $\theta_c = 45°$. In our current analysis, we use Eqs. (4,7,8) with $\theta_c = 110°$ (similar to the experiments [10,16]) to find $p_{c,max}$.

2.2. Meniscus simulation based on energy minima

The Surface Evolver (SE) code [14] uses the principle of energy minimization to iteratively determine the meniscus topology. The SE simulates the meniscus and the solid surface, so it does not require a volume mesh. Since here the Bond number is small (for the range of particle diameters leading to condensation enhancement), the effect of the gravity is negligible. The mesh size was selected so as to have at least 64 cells at the particle circumference and the conjugate gradient method was used to achieve faster convergence. The methodology used to create the geometry and mesh is similar to that used in [9].

The total energy combines the contact line, meniscus surface, and the liquid body energies, i.e.,

$$E = \int \boldsymbol{F}_e.d\boldsymbol{l} + \int\int \boldsymbol{\sigma}_{ij}.d\boldsymbol{A} + \int\int\int f_b dV, \tag{9}$$

where $\boldsymbol{F}_e$ is the contact line tension vector, $\boldsymbol{\sigma}_{ij}$ is the interfacial tension between phase i and j, and $f_b = \rho g z$ when the gravity is considered [14]. A video of predicted meniscus dynamics is linked to Figure 4, and the snapshots are shown there.

2.3. Meniscus spouting, droplet formation and growth

The transport of liquid within the monolayer wick follows two regimes: (a) the meniscus grows passing through the pore throat becoming unstable, i.e., spouting, and coalesces with the adjacent menisci and other droplets that have already formed on the particle surface outside the meniscus to form a droplet, and (b) the droplet continues to grow by receiving liquid from the adjacent pores followed by coalescence with other droplets present on the monolayer. At the end of the second regime, the droplet becomes large enough to begin traveling down the surface due to the gravity. The analysis leading to these results is described below. The intrinsic contact angle is 110° similar to the hydrophobic coating used in the experiment of [10,16] and those reported here.

In the first regime, condensation at the meniscus causes it to grow and the capillary pressure to increase. After the meniscus passes through the pore neck (or throat), the capillary pressure begins to decrease. With further liquid (droplet) volume increase, the capillary pressure decreases further, until it becomes smaller than that of the surrounding menisci, which have yet to transition through the neck. This pulls liquid from the surrounding regions into the meniscus, causing its volume to increase and its capillary pressure to fall further. This volume rise is sudden and leads to spouting and coalescence with other menisci to form a droplet at the end of the first

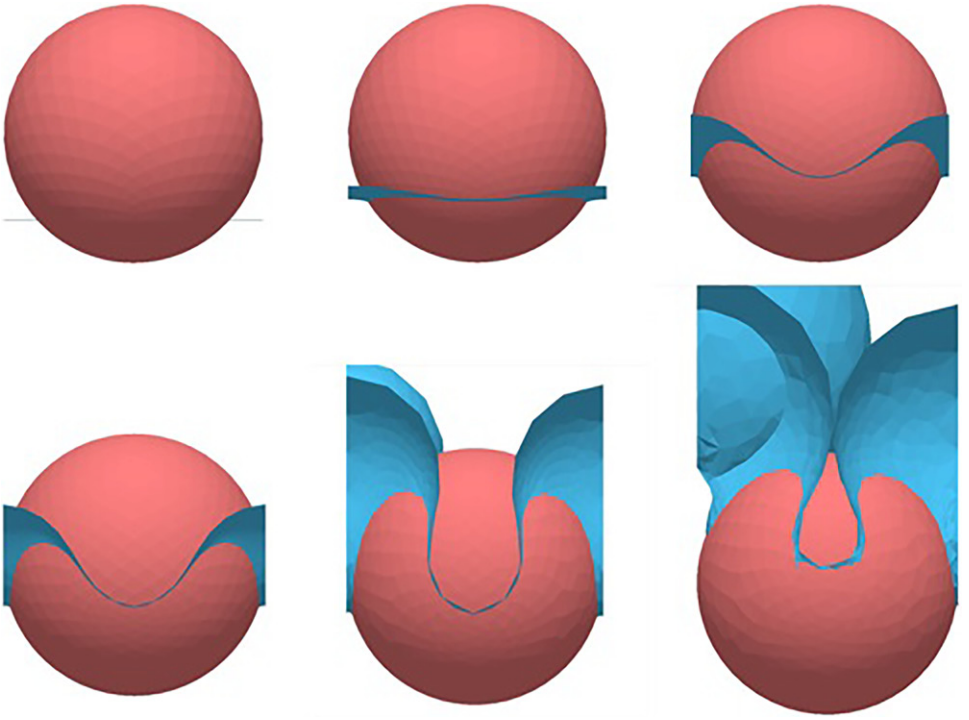

Figure 4. Video showing the pore condensate growth regimes predicted with the SE simulations, for contact angle of 110°. https://www.youtube.com/watch?v=vA_6hLN7hqc.

regime, as shown in Figure 5*a*. In the second regime, the droplet continues to receive liquid from the surrounding menisci and continues to grow, as is shown in Figure 5*b*, until the droplet is large enough to depart due to the gravity. This mechanism of meniscus spouting and pore emptying has also been observed in nanopores [17].

In this study, the variation of the capillary pressure with the meniscus topology is analyzed and an analytical relation is developed. The estimated p_c has been plotted against the meniscus contact line apex angle in Figure 6*a*. The SE results are used for the relation between s_l and α. Using this relation, the analytical and numerical estimates for p_c with respect to s_l are shown in Figure 6*c*. The position of the meniscus corresponding to $p_c = 0$ is the equilibrium position of the meniscus. When the meniscus volume falls below the equilibrium, then p_c becomes negative, causing the meniscus to receive liquid from the surrounding menisci and regain its equilibrium. Similarly, when the meniscus volume increases, then p_c becomes positive, forcing the meniscus to pass liquid to the adjacent menisci and return to its equilibrium. The s_l and α corresponding to the equilibrium position are denoted as s_l and α_e in Figure 6*b*. When the meniscus volume rises above $s_{l,max}$, i.e., $s_l > s_{l,max}$ and $\alpha > \alpha_{max}$, the capillary pressure gradient (with respect to α) becomes negative. Then the p_c no longer enables the meniscus to return to its equilibrium position and the meniscus volume has to increase for the capillary pressure to decrease, as indicated by Figure 6*a*. The meniscus then collects liquid from its surroundings and grows and spouts, as discussed above. The liquid expelled by the monolayer wick through the spouting forms the surface droplet.

2.4. Droplet departure on smooth surface

Once the droplet reaches the departure volume, it begins to move down the vertical surface while it continues to add liquid from the menisci underneath it and by coalescence with the

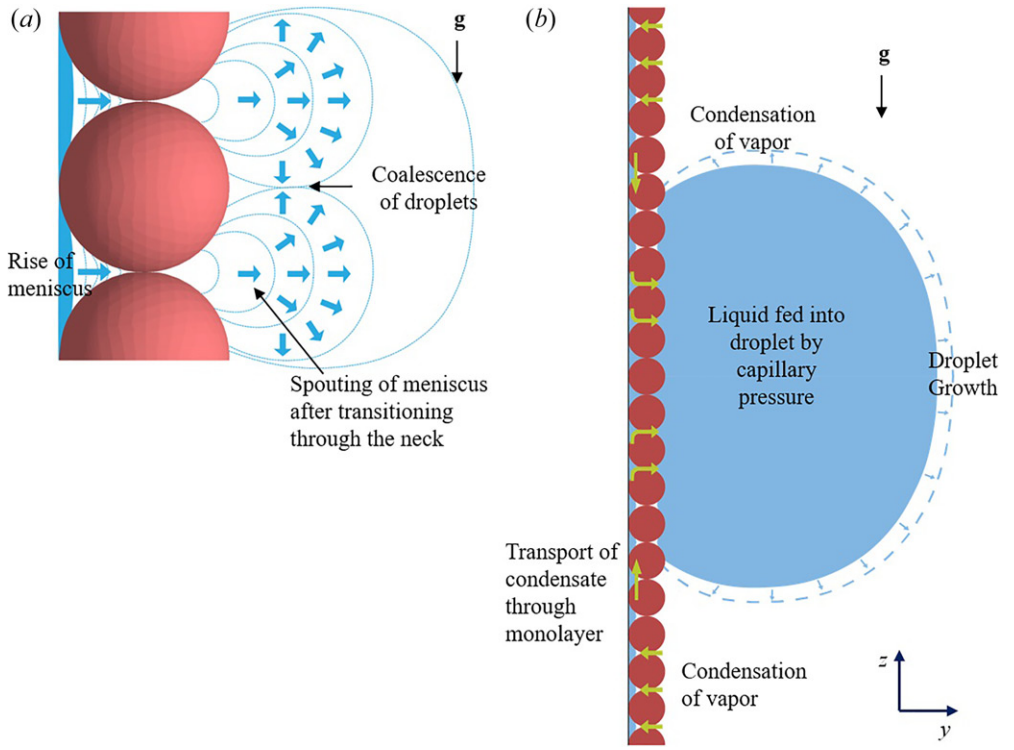

Figure 5. (*a*) Mechanism of meniscus pore filling, spouting, and droplet formation in the wick regime. (*b*) Mechanism of liquid transport through the monolayer and the droplet growth.

neighboring droplets in its path. The departing droplet volume on a smooth vertical hydrophobic surface has been estimated using the SE code [14]. The simulation accounts for the contact angle and the effect the gravity. The minimum droplet departure volume is denoted as the critical volume. As the droplet volume approaches the critical volume, the capillary pressure in the droplet begins to diverge as in Figure 7*a*. The droplet volume at this point is considered to be the departing droplet volume and is 3.7 µL. This critical diameter of 2100 µm (the SE simulation geometry is shown in Figures 7*b* and 7*b*), is in close agreement with the results of [18]. The Bond number (Bo_d) shown in Figure 7*a*, is define as

$$\mathrm{Bo}_d = \Delta\rho_{lg} g d_d^2/\sigma. \tag{10}$$

A snapshot of the SE simulation of the droplet sliding down the smooth surface is shown in Figures 7*b* and 7*c*, with the contact angle of 110°. Equation (8) predicts that the pressure required for the meniscus to spout is over ten times larger than the capillary pressure in the departing droplet (or other similar surface droplets) in the particle-size range considered ($d_p < 500\,\mu\mathrm{m}$). Therefore, the menisci are more likely to remain stationary, passing condensate laterally through the monolayer to the adjacent pores experiencing meniscus spouting (and connected to droplet over the monolayer wick), as shown in Figure 5*b*. This assumption about the meniscus maintaining a constant thickness is used in the thermal resistance calculation.

3. Numerical analysis of heat transfer in the monolayer wick

The droplet ensemble-level condensation is assumed to occur in a quasi-static manner and is rendered in Figure 8.

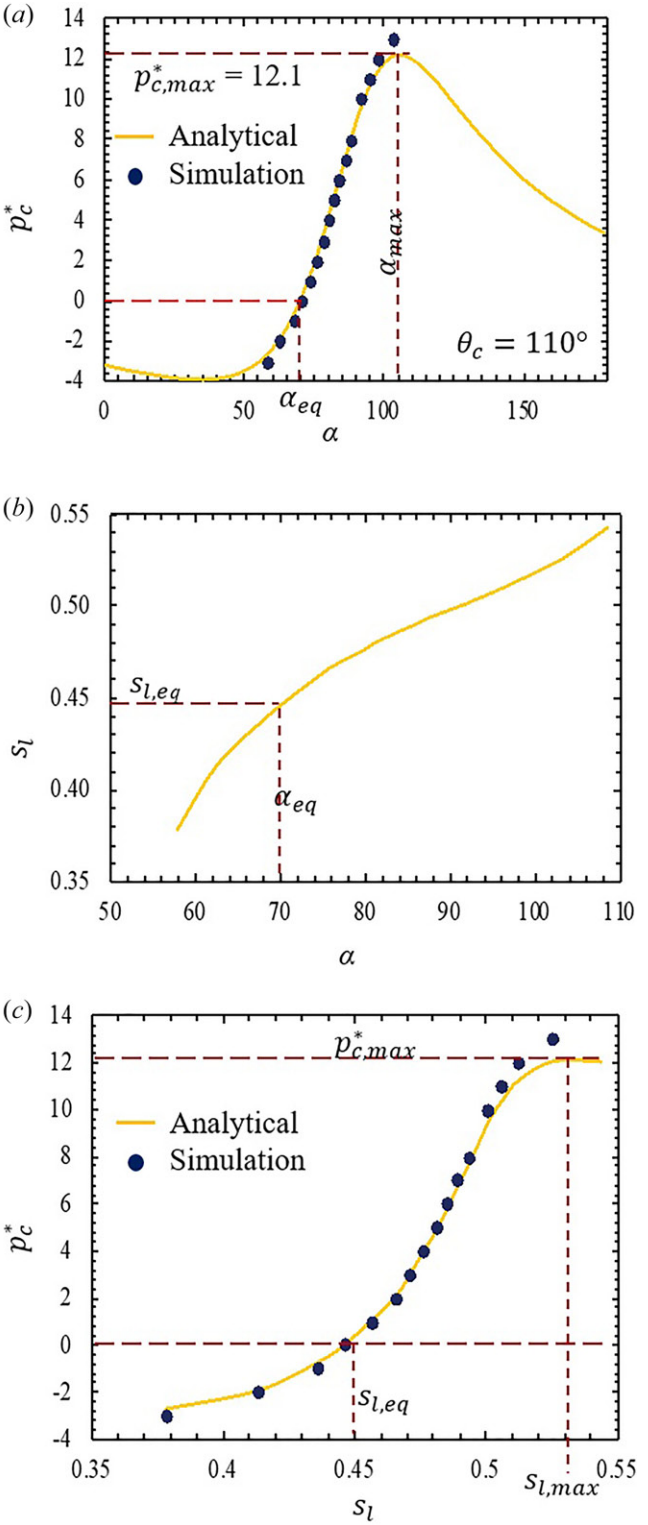

Figure 6. (*a*) Variations of the capillary pressure with the contact line apex angle. (*b*) Variations of the liquid volume fraction with the contact-line apex angle. (*c*) Variations of the capillary pressure with the pore liquid volume fraction (liquid saturation).

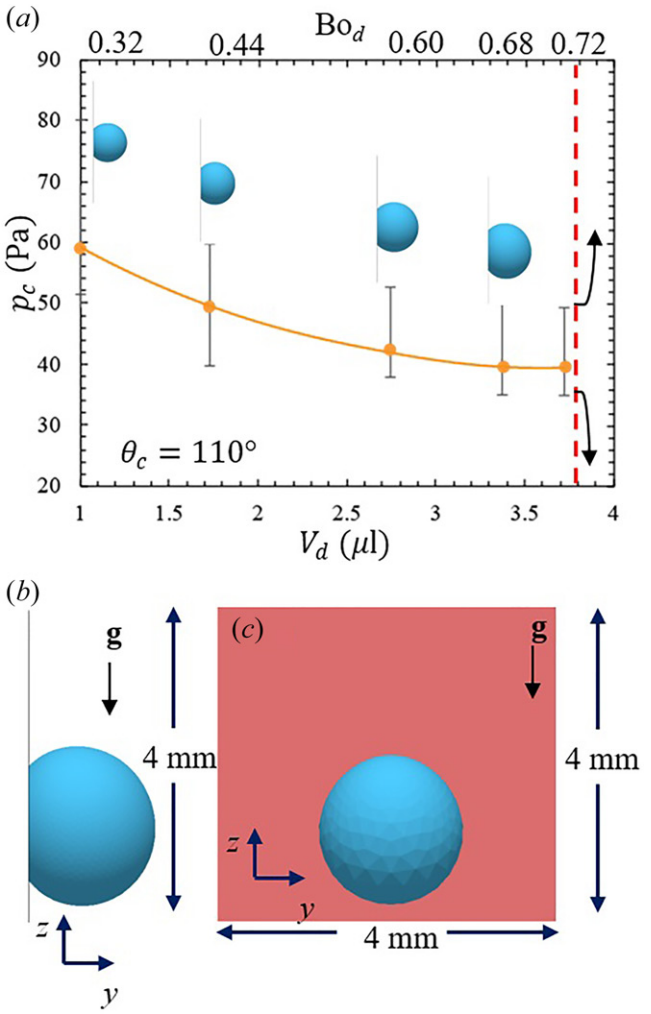

Figure 7. (*a*) Variations of the capillary pressure with the pore liquid volume. The maximum and minimum of the fluctuating pressure diverge after the droplet reaches the critical volume. The droplet geometry on a smooth vertical plate is also shown with (*b*) side, and (*c*) front views.

The heat transfer analysis is divided into three regimes, depending on the particle diameter, namely, the roughness regime ($d_p \leq 4\,\mu$m), the wick regime ($4\,\mu\text{m} < d_p \leq 6{,}200\,\mu$m), and the fin regime ($d_p > 6{,}200\,\mu$m), and these are described below, starting with the dominant (wick) regime. The estimated particle size ranges for these three regimes are shown in Figure 9 along with the rendering of condensate in each regime. The experimental results of [10] and those listed in Appendix A, are also shown. The results for the inverse of the heat transfer coefficient (AR, where R is the condensation resistance) made dimensionless with respect to the experimental plain surface result AR_{ps}.

3.1. Wick regime

The wick regime is the most important regime from the perspective of microstructured surfaces, because the microstructure affects both the formation and the transport of the condensate. As stated above, this regime becomes dominant in the particle size range starting from a few microns

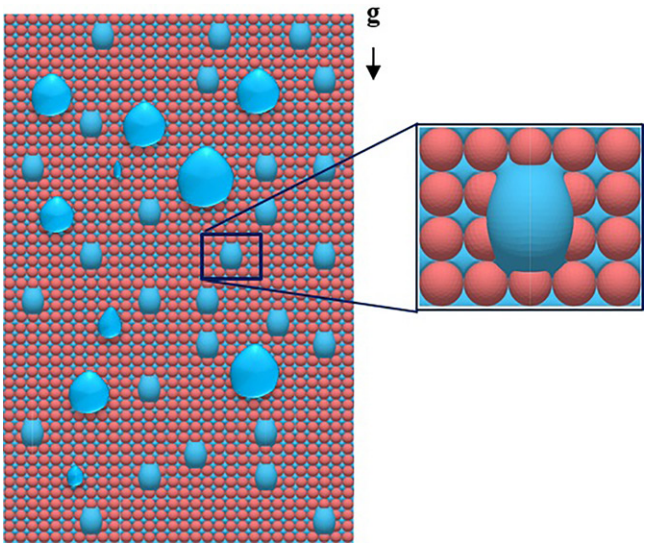

Figure 8. Rendering of the ensemble-level dropwise condensation over the hydrophobic sintered particle monolayer wick.

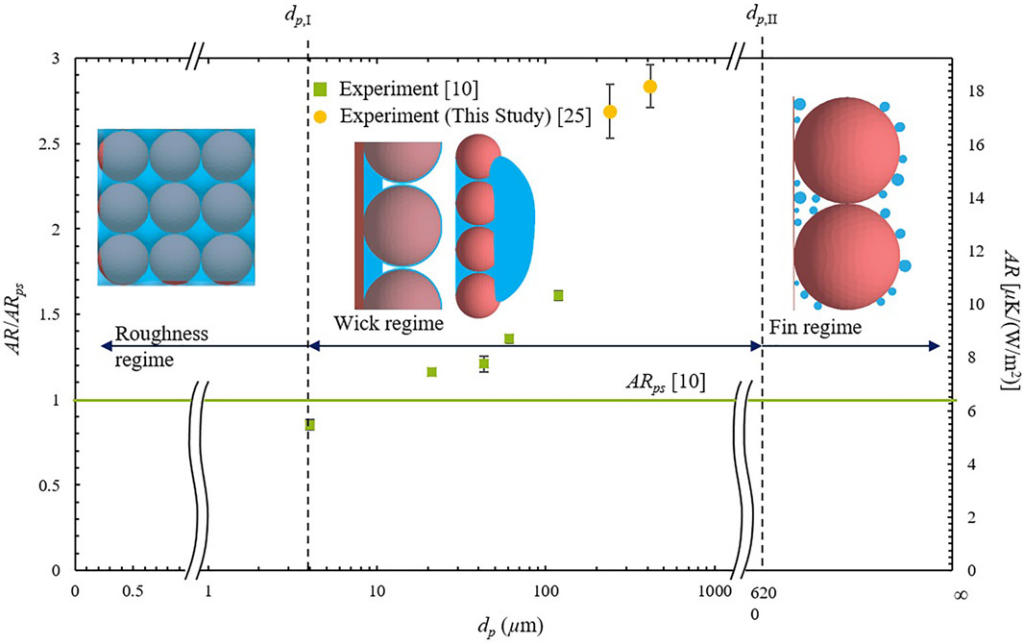

Figure 9. Variations of the dimensionless dropwise condensation resistance (made dimensionless using the plain surface results) with respect to the monolayer particle diameter/three regimes and their ranges are identified, namely, the surface-roughness, wick and fin regimes. The experimental results of [10] and additional results from Appendix A are also shown.

and lasts until particle sizes of hundreds of microns. In general, it is challenging to fabricate homogeneous particle packing in the monolayer for sub-micron particles, so the control the condensate transport is greatly reduced. On the other side, for particles around millimeter, the capillarity is significance reduced.

The condensation in the wick regime is composed of three sub-regimes that occupy different fractions of the surface area, namely, the coverage regime, the flood regime and the pore

regime. The area fraction occupied by each regime is determined by the droplet size distribution. In this analysis, we assume the droplet distribution to follow the correlation developed in [19]. Each regime has unique heat transfer characteristics which are discussed below.

The coverage sub-regime is characterized by droplets with $d_d > d_{d,c} = 0.2\,\text{mm}$ which are assumed to be perfectly insulating due to the relatively low conductivity of water [5]. The coverage sub-regime occupies an area fraction, x_c on the condensing surface. The x_c based on the Rose's model [19] is found as

$$x_c = 1 - \left(d_{d,c}/d_{d,max}\right)^{1/3}, \tag{11}$$

The remaining area $[A(1 - x_c)]$ is responsible for all the heat transfer and condensation and is assumed to be covered by the other two regimes having smaller droplet sizes ($d_d < d_{d,c} = 0.2\,\text{mm}$). Of the other two regimes, the flood regime consists of droplets that bridge across two or more particles but are smaller than $d_{d,c}$ i.e $d_{d,flood} < d_d < d_{d,c}$, where $d_{d,flood}$ is found for an HCP particle arrangement as

$$d_{d,flood} = \left(2/3^{1/2} - 1\right) d_p. \tag{12}$$

The area fraction occupied by this regime x_{flood} depends on $d_{d,flood}$, which depends on d_p, thus making x_{flood} dependent on d_p. the area fraction x_{flood} is calculated as

$$x_{flood} = \left(d_{d,c}^{1/3} - d_{d,flood}^{1/3}\right)/d_{d,max}^{1/3}, \tag{13}$$

And the average droplet size in this regime, $\langle d_{d,flood} \rangle$ is found as

$$\langle d_{d,flood} \rangle = \left(d_{d,c}^{4/3} - d_{d,flood}^{4/3}\right)/\left[4\left(d_{d,c}^{1/3} - d_{d,flood}^{1/3}\right)\right], \tag{14}$$

In the flood regime, the bridged droplets block the pores, preventing the vapor to reach and condense on the meniscus. The condensation therefore occurs on the surface of the droplets and the thermal resistance is therefore dependent on $\langle d_{d,flood} \rangle$.

The pore sub-regime consists of droplets that are small enough to be contained on a single particle ($d_d < d_{d,flood}$) . The area fraction occupied by this regime is calculated as

$$x_{pore} = 1 - x_c - x_{flood}, \tag{15}$$

And the average droplet size in this regime is

$$\langle d_{d,pore} \rangle = d_{d,flood}/4. \tag{16}$$

As mentioned earlier, it can be inferred from Eqs. (11,13,15) that x_c is independent of the d_p and depends only on the departing droplet diameter $d_{d,max}$, while x_{flood} and x_{pore} depend on d_p and $d_{d,max}$. These predicted area fractions are shown in Figure 10.

3.2. Heat transfer characteristics of the three sub-regimes

To estimate the heat transfer, we approximate the droplets to be a uniform liquid film, which would have the same thermal resistance as spherical-cap droplet, shown in Figure 11. The relation between the droplet diameter and the corresponding film thickness is found from numerical simulations using the Star CCM + software, giving $\langle \delta_{l,f} \rangle = 0.09 \langle d_d \rangle$ for spherical-cap droplets and the relation is independent of d_d. The simulation use a mesh size of $0.01 d_d$ with a denser mesh in the contact region, since most of the heat transfer occurs there. The mesh independence was confirmed by considering mesh size of $0.008 d_d$ and $0.012 d_d$ and the results varied < 2%. The boundary conditions and the temperature distribution are shown in Figure 11. The boundary condition $1/AR_{l\text{-}g}$ accounts for the liquid–vapor interfacial thermal resistance, which is taken as $0.2\,\mu\text{W}/(\text{m}^2\text{-K})$ at one atm pressure for water (http://www.thermopedia.com/content/652/).

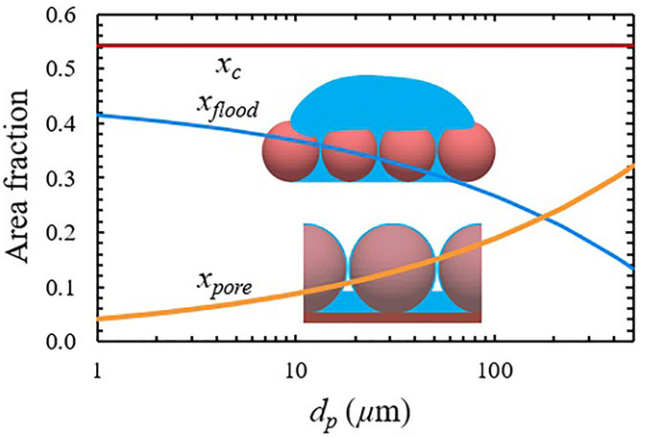

Figure 10. Variations of the area fraction occupied by the pore, the flood and the coverage regimes, with respect to the particle diameter.

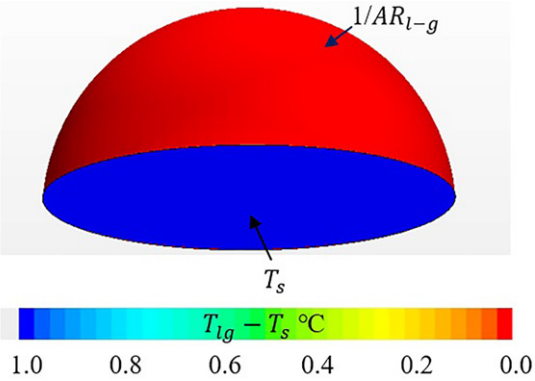

Figure 11. The simulated temperature distribution for a surface spherical-cap droplet, and the boundary conditions used for the heat transfer simulations.

The contribution of the coverage regime towards the heat transfer is considerably smaller owing to the larger droplets, and therefore, is neglected.
The flood sub-regime droplets are approximated with a uniform film thickness

$$\langle \delta_{l,flood} \rangle = 0.052 \langle d_{d,flood} \rangle, \tag{17}$$

and the thermal resistance is the sum of the resistance offered by the droplets and the monolayer beneath them as

$$AR_{flood} = \langle \delta_{l,flood} \rangle / k_l + c_{flood} d_p / k_{\mathrm{Cu}}, \tag{18}$$

with the constant c_{flood} accounting for the constriction (at the contact particle base and the heat path traveled to reach the flooded droplets)

$$c_{flood} = 4\ln\{[\sin\theta_c(1+\cos\theta_0)]/[\sin\theta_0(1+\cos\theta_c)]\}/(3^{1/2}\pi), \tag{19}$$

where

$$\theta_0 = \sin^{-1}(d_c/d_p). \tag{20}$$

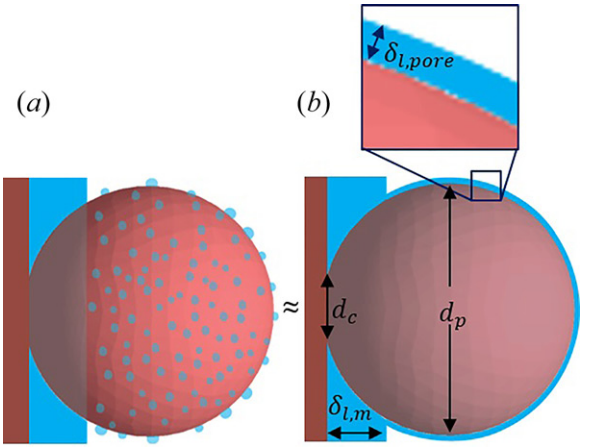

Figure 12. (a) Rendering of the meniscus and small droplets formed on the particle surface. (b) Approximation of the droplets on the particle surface as a thin film with uniform thickness.

The magnitude of c_{flood} is 1.95 and 1.07 for the contact diameter ratios of $d_c/d_p = 0.2$ and 0.6, respectively.

Similarly the average droplet diameter for the pore sub-regime (unbridged droplets) is

$$\langle d_{d,pore} \rangle = d_{d,flood}/4, \tag{21}$$

and the pore droplets are approximated to be a uniform film as shown in Figure 12, with thickness

$$\langle \delta_{l,pore} \rangle = 0.09 \langle d_{d,pore} \rangle, \tag{22}$$

and the thermal resistance offered by the droplets is

$$\langle AR_{d,pore} \rangle = \langle \delta_{l,pore} \rangle / k_l. \tag{23}$$

The heat transfer in the pore regime occurs through the meniscus and the particle surface above the meniscus (which is covered by the unbridged droplets with $\langle d_{d,pore} \rangle$). The heat transfer in this regime depends not just on the average thickness of the droplets on the particle surface but also on the meniscus thickness $\langle \delta_{l,m} \rangle$. To determine $\langle \delta_{l,m} \rangle$, consider the capillary pressure in the meniscus controlled by the capillary pressure of the droplets that form above the monolayer. From Eq. (1), the smallest capillary pressure occurs when the droplets reach the departure diameter, i.e.,

$$p_c = 4\sigma \cos\theta_c / d_{d,max} = 40 \text{ Pa}. \tag{24}$$

We assume that droplets near the departure size are spread uniformly across the entire surface and hence the liquid in the menisci also have $p_c = 40$ Pa. Using the SE simulations and Eq. (4), for $p_c = 40$ Pa, $s_l \approx s_{l,eq}$ when $4\,\mu\text{m} \le d_p \le 500\,\mu\text{m}$. The average meniscus thickness $\langle \delta_{l,m} \rangle / d_p$ is determined from s_l using

$$s_l = \left\{ \left(3^{1/2} \langle \delta_{l,m} \rangle / d_p \right) - \pi \left(\langle \delta_{l,m} \rangle / d_p \right)^2 \left(1 - 2\langle \delta_{l,m} \rangle / 3d_p \right) \right\} / \left(3^{1/2} - \pi/3 \right). \tag{25}$$

Using Eq. (25), we find $\langle \delta_{l,m} \rangle / d_p = 0.33$, when $s_l \approx s_{l,eq}$. since the heat transfer paths through the meniscus and through the droplets on the particle surface outside the meniscus are complex, the net heat transfer is estimated numerically.

The steady-state pointwise energy equation with heat conduction in the wick (solid, spherical copper particles and liquid water) is solved numerically using the Star CCM + software. Several studies have numerically modeled heat transfer through micro-structures such as micro fins [20,21] and helical fins in micro channels [22]. The unit-cell, surface hexagonal close packing

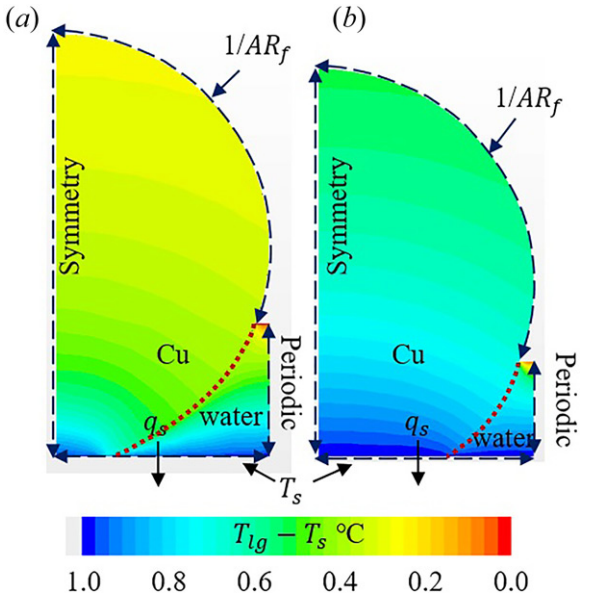

Figure 13. The simulated temperature distributions in the liquid meniscus and in the substrate-sintered particle. The boundary conditions are also shown for the two different particle-substrate sintering extent of (a) $d_c/d_p = 0.2$, and (b) 0.6.

(HCP) is used with periodic and symmetry boundary conditions, as shown in Figure 13. The energy equation, the conduction heat flux vector $\boldsymbol{q}$, and the boundary conditions are

$$\nabla.\boldsymbol{q} = 0, \quad \boldsymbol{q} = -k\nabla T, T \text{ or } AR \text{ prescribed on the boundaries} \tag{26}$$

The particle sintering to the substrate was simulated with sintering diameter (d_c) of $0.6d_p$ and $0.2d_p$. The actual sintering diameter is expected to lie within these under moderate sintering. The mesh independence was verified using progressively smaller mesh size of 0.022, 0.020 and $0.018d_p$ and the variation in the heat transfer rate was less $< 2\%$.

The substrate surface temperature T_s was assumed to be 1 °C below the liquid-vapor saturation temperature T_{lg} imposed on the meniscus surface. A heat transfer coefficient boundary has been imposed on the exposed particle surface representing a liquid film. The average meniscus thickness $\langle \delta_{l,m} \rangle$ is determined from Eq. (25) and d_p. The assumed film on the particle is related to the heat transfer coefficient boundary as

$$AR_f = AR_{d,pore} + AR_{l-g}, \tag{27}$$

where $AR_{l\text{-}g}$ is the interfacial thermal resistance, which has been found to be 0.2 μK/(W/m^2). The thermal resistance of the pore sub-regime is equal to the resistance of the unit cell is

$$\langle AR_{pore} \rangle = \left(T_{lg} - T_s\right)/\langle q_s \rangle. \tag{28}$$

The pore, the flood and the coverage sub-regimes are parallel heat-flow paths, so the combined thermal resistance for the surface in the wick regime is

$$1/AR_{mw,c} = \left(x_{pore}/\langle AR_{pore} \rangle\right) + \left(x_{flood}/\langle AR_{flood} \rangle\right). \tag{29}$$

The coverage regime does not contribute much to the heat transfer and is therefore excluded from Eq. (29).

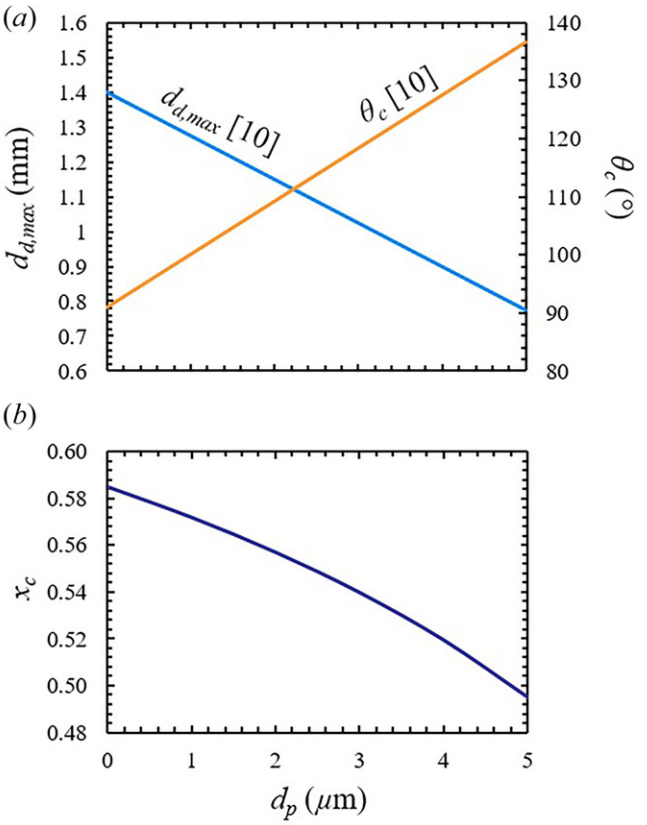

Figure 14. (a) Variations of θ_c and $d_{d,max}$ with d_p in the surface-roughness regime. (b) Decrease in x_c with an increasing d_p.

3.3. Surface-roughness regime

When the particle size reduces below approximately 4 μm (observed experimentally in [10]), they can be treated as random undulations instead of an ordered surface packing of the particle, and this is approximated as surface roughness. The wick also has little effect on heat transfer from the surface, because the bridged droplets occupy over 95% of the surface area and hence are the dominant factor in determining the overall thermal resistance (so their contribution is neglected)/However the undulations on the surface (surface roughness) can still promote dropwise condensation by increasing the apparent contact angle of hydrophobic surfaces as observed in [23]. The increase in contact angle reduces the droplet departure size resulting in lower x_c and a lower average droplet size as is evident from the Rose model [18]. The lower coverage increases the area fraction available for condensation, reducing the thermal resistance of the surface. We assume that the improvement in heat transfer is proportional to the uncovered area fraction (1- x_c) and is

$$A_{mw,c}/A_{ps} = (1-x_{c,mw})/(1-x_{c,ps}), \tag{30}$$

where x_c is calculated from $d_{d,max}$ using Eq. (11). The $d_{d,max}$ is calculated using the contact angles observed by [10] and the corresponding $d_{d,max}$ found by [17]. The increase in θ_c leads to in $d_{d,max}$ as shown in Figure 14a and the resulting decrease in x_c in Figure 14b.

3.4. Fin regime

In the fin regime, the dropwise condensation occurs at the substrate interface as well as the vapor-exposed particle surface. A stable meniscus is not able to form, because the critical pressure

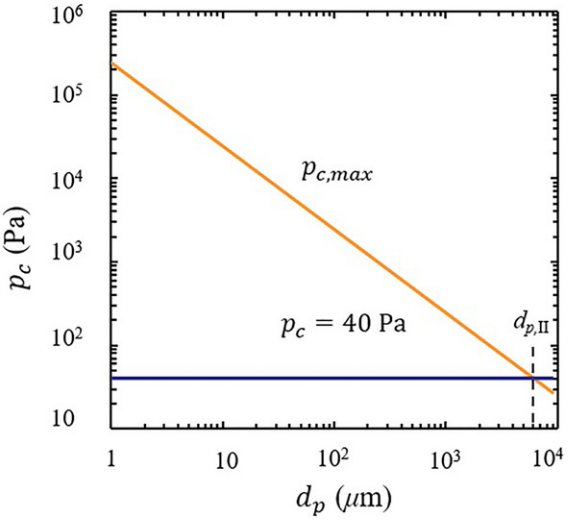

Figure 15. Variation of the maximum capillary pressure with d_p, leading to the determination of $d_{p,II}$.

of the monolayer (inversely proportional to d_p) becomes smaller than the minimum meniscus capillary pressure of 40 Pa, as shown in Figure 15. The particle diameter for this transition is denoted as $d_{p,II}$, so the fin regime covers $d_p \geq d_{p,II}$, or $p_{c,max} \leq 40$ Pa. Then the $d_{p,II}$ is determined using Eqs. (7, 8, 24) and is found to be 6200 μm.

The thermal resistance of the monolayer in this regime is modeled noting that heat travels directly through the substrate as well as the particles. This is assumed to flow through the particle in straight lines from the point of contact to the surface of the particle. The average path length for the heat to travel is equal to the average chord length calculated from the base of the particle to the surface. The average path length is found by taking the surface area weighted mean of the chord lengths, as shown in Figure 16, i.e.,

$$\langle l_k \rangle = \left\{ \int_0^{\pi} l_k dA \right\} / \int_0^{\pi} dA = 2d_p/3, \tag{31}$$

where $l_k = 2d_p \sin\left(\frac{\beta}{2}\right)$ and $dA = \frac{\pi}{2} d_p^2 \sin(\beta) d\beta$ is the differential surface area that subtends an angle of $d\beta$ on the center of the particle.
The average cross-sectional area of the particle is $\pi(d_p/2)^2$ and thermal resistance offered by the copper particle is

$$AR_k = 8d_p/3\pi k_{\mathrm{Cu}}. \tag{32}$$

The resistance for condensation on the substrate surface is the plain surface result, AR_{ps}. The heat path through the particle is in parallel with the heat path though the substrate surface, i.e,

$$1/AR_{mW,c} = 1/AR_{ps} + 1/\left(AR_k + AR_{ps}/\pi\right). \tag{33}$$

For $d_p \to \infty$, AR_k becomes very large, and therefore, $AR_{m,c} \to AR_{ps}$.
In this regime, the monolayer does not show any wicking effect, and has a fin-type behavior instead. This fin effect is not pursued here.

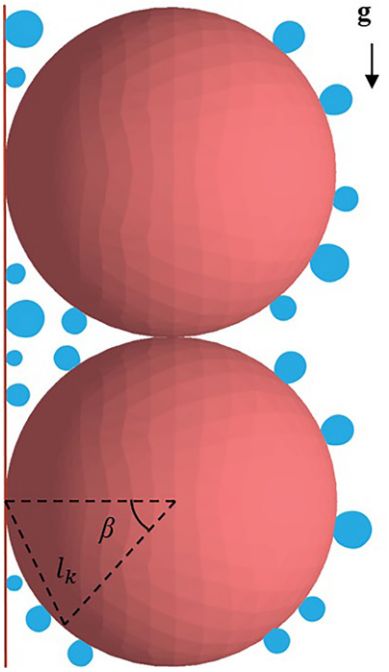

Figure 16. Rendering of the condensation mechanisms for particles larger than the critical particle diameter, showing dropwise condensation on the substrate and on the particle surface, with no meniscus formation on the substrate.

4. Results and discussion

Figure 17 summarizes the predicted dropwise condensation resistance with the monolayer wick, in comparison to the experimental results [10, 16, also Appendix A]. Also shown is the resistance of 1 mm of copper, a measure of a small and relevant substrate resistance, for comparison.

As $d_p \rightarrow 0$, the plain-surface behavior is approached, influenced by the surface roughness which increases the apparent contact angle. A higher contact angle lowers $d_{d,max}$, thus reducing x_c and results in a marginally lower thermal resistance.

For the $d_p > d_{p,\mathrm{I}}$, the microstructure becomes dominant and pores begin to open to condensation allowing meniscus formation within the monolayer and leading to the wick regime. A marginal enhancement is observed in this regime due to the additional area imparted by the curved particle surface for condensation, a small meniscus thickness and a higher apparent contact angle than the plain surface as observed in [10]. However, as d_p increases, the meniscus thickness increases, raising the thermal resistance of the wick. Furthermore, the apparent contact angle begins to decrease and the particles hinder the gravity driven sweeping of the large droplets as observed in the results presented in Appendix A, leading to a higher x_c, and causing the net resistance to rise.

The monolayer shows a marginal improvement in the heat transfer performance when $d_p < 50\,\mu\mathrm{m}$. For $d_p > d_{p,\mathrm{II}}$, the mechanism of liquid transport changes as discussed in Section 3. In this regime, the particles shows fin-type behavior and are unable to function as a wick owing to much reduced capillarity. This regime may show some heat transfer enhancement, however the fin-type behavior of large particles is not considered here. In the limit of $d_p \rightarrow \infty$, the resistance offered by the particles becomes large enough to prevent any heat transfer through them thus allowing condensation only on the substrate. This causes the resistance to return to the plain surface value.

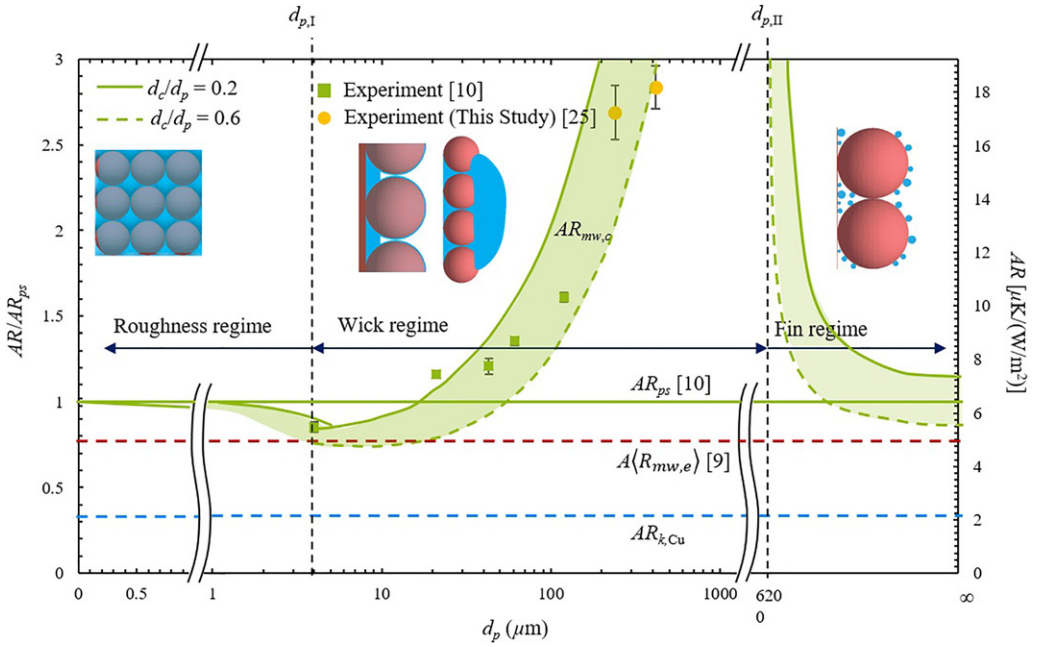

Figure 17. Predicted thermal resistance found using the parallel heat path model (wick regime) with respect to the particle size. The behavior of $AR_{\Sigma,c}$ in the limits of $d_p \to 0$ (roughness regime) or ∞ (fin regime) are also shown. $AR_{mw,e}$ is for the evaporation monolayer wick [9]. The resistance of 1 mm of copper, $AR_{k,\mathrm{Cu}}$, is also shown for comparison.

5. Conclusions

In search of further dropwise condensation enhancement, surface microstructures have been considered in many investigations. We numerically analyzed the vertical-plate dropwise condensation phenomenon over a sintered-particle, hydrophobic monolayer with condensation on the meniscus in the monolayer and over the particle surface above the meniscus. The meniscus dynamics is tracked using the interfacial tension forces and the capillary pressure subject to the minimum meniscus surface energy. This is used in the treatment of the liquid and the heat transport within the wick and the formation and growth of the condensate droplets over the surface. We use a bimodal distribution which captures the droplet distribution effect by neglecting the heat transfer through larger droplets. The heat transfer mechanism depends on the particle diameter as explained in Section 4. The predicted resistance is lower than the experiments, partly due to the differences between the homogenous packed particles that were assumed in the analysis and the heterogeneously packed particles that were fabricated and tested in the experiments.

Under homogeneous particle packing, we predict that the heat transfer can be enhanced by up to 25% using the monolayer wick, compared to the plain surface. The extent of enhancement depends on the particle sintering and packing. The monolayer hinders the gravity-driven sweeping of the large droplets, rendering a large portion of the surface unavailable for condensation, resulting in a modest enhancement which persists over $15 < d_p < 50\,\mu$m. This is similar to the results reported in [24]. This attests to the limited ability of the microstructures to enhance dropwise condensation on hydrophobic surfaces, and attributes this to the tendency of the microstructured surfaces to flood under high heat flux. Thicker wicks (i.e., porous media), suppress dropwise condensation and deteriorate filmwise condensation enhancement with additional thermal resistance [25].

The heat transfer characteristics of the monolayer wick for the particle diameter approaching zero resemble that over a plain surface, i.e., the meniscus is formed over the particles and floods the pores. In the large particle-diameter limit: (a) the meniscus is unable to form within the

monolayer and condensation occurs on the substrate and over the particle surface (similar to a plain surface), and (b) the particles do not show a wicking effect (but there will be a fin-effect enhancement)

Acknowledgments

The authors would like to thank Phil Martin (ACT) for his experimental testing expertise. Minki Kim (UM) assisted in starting the simulations with the Surface Evolver.

Funding

This work was funded by the Office of Science in the U.S. Department of Energy (DOE) under a Regime II SBIR grant, Award Number DE-SC-0011317 (Program Manager: Robie Lewis).

References

[1] J. W. Rose, "Dropwise condensation theory and experiment: a review," *J. Power Energy*, vol. 216, no. 2, pp. 115–128, 2002. DOI: 10.1243/09576500260049034.

[2] R. W. Bonner, "Correlation for dropwise condensation heat transfer: Water, organic fluids, and inclination," *Int. J. Heat Mass Transfer*, vol. 61, pp. 245–253, 2013. DOI: 10.1016/j.ijheatmasstransfer.2012.12.045.

[3] E. J. Le Fevre, and J. W. Rose, "An experimental study of heat transfer by dropwise condensation," *Int. J. Heat Mass Transfer*, vol. 8, no. 8, pp. 1117–1133, 1965. DOI: 10.1016/0017-9310(65)90139-0.

[4] R. Leach, F. Stevens, S. Langford, and J. Dickinson, "Dropwise condensation: Experiments and simulations of nucleation and growth of water drops in a cooling system," *Langmuir*, vol. 22, no. 21, pp. 8864–8872, 2006. DOI: 10.1021/la061901+.

[5] B. Mikic, "On mechanism of dropwise condensation," *Int. J. Heat Mass Transfer*, vol. 12, no. 10, pp. 1311–1323, 1969. DOI: 10.1016/0017-9310(69)90174-4.

[6] B. Qi, Z. Song, and X. Li, "Numerical study on condensation heat transfer of trapezoid grooved surfaces," *Adv. Mech. Eng.*, vol. 8, no. 5, pp. 1–11, 2016. DOI: 10.1177/1687814016648247.

[7] M. Izumi, S. Kumagai, R. Shimada, and N. Yamakawa, "Heat transfer enhancement of dropwise condensation on a vertical surface with round shaped grooves," *Exp. Thermal Fluid Sci.*, vol. 28, no. 2–3, pp. 243–248, 2004. https://doi.org/10.1016/S0894-1777(03)00046-3 DOI: 10.1016/S0894-1777(03)00046-3.

[8] D. Chatain, D. Lewis, J. Baland, and W. Carter, "Numerical analysis of the shapes and energies of droplets on micropatterned substrates," *Langmuir*, vol. 22, no. 9, pp. 4237–4243, 2006. DOI: 10.1021/la053146q.

[9] M. Kim, and M. Kaviany, "Multi-artery heat pipe spreader: Monolayer wick receding meniscus transitions and optimal performance," *Int. J. Heat Mass Transfer*, vol. 112, pp. 343–353, 2017. DOI: 10.1016/j.ijheatmasstransfer.2017.04.131.

[10] S. Hoenig, and R. W. Bonner, "Dropwise condensation on superhydrophobic microporous wick structures", *ASME J. Heat Transfer*, vol. 140, no. 7, pp. 071501–071501, 2018. DOI: 10.1115/1.4038854.

[11] M. Kaviany, *Principles of Heat Transfer in Porous Media*, 2nd ed. New York, NY, Springer, 1995. https://link.springer.com/book/10.1007%2F978-1-4612-4254-3.

[12] M. C. Leverett, "Capillary behavior in porous solids," *Trans. AIME*, vol. 142, no. 1, pp. 152–169, 1941. DOI: 10.2118/941152-G.

[13] J. C. Melrose, "Wettability as related to capillary action in porous media," *Soc. Petrol. Eng. J.*, vol. 5, no. 3, pp. 259–271, 1965. DOI: 10.2118/1085-PA.

[14] K. A. Brakke, "The surface evolver," *Exp. Math.*, vol. 1, no. 2, pp. 141–165, 1992. DOI: 10.1080/10586458.1992.10504253.

[15] S. G. Liter, and M. Kaviany, "Pool-boiling CHF enhancement by modulated porous-layer coating: Theory and experiment," *Int. J. Heat Mass Transfer*, vol. 44, no. 22, pp. 4287–4311, 2001. DOI: 10.1016/S0017-9310(01)00084-9.

[16] S. Hoenig, and R. W. Bonner, "Dropwise condensation on hydrophobic microporous powder and the transition to intrapowder droplet removal," 3rd Thermal Fluids Engineering Conference, Fort Lauderdale, FL., 2018, pp. 643–653, 2018. DOI: 10.1615/TFEC2018.ens.020457.

[17] M. Knezevic, and J. M. Yeomans, "Pore emptying transition during nucleation in hydrophobic nanopores," *Soft Matter*, vol. 12, pp. 3810–3819, 2016. DOI: 10.1039/C6SM00148C.

[18] C. H. Lu *et al.*, "Heat transfer model of dropwise condensation and experimental validation for surface with coating and groove at low pressure," *Heat Mass Transfer*, vol. 52, no. 1, pp. 113–126, 2016. DOI: 10.1007/s00231-015-1641-0.
[19] J. W. Rose, and L. R. Glicksman, "Dropwise condensation: The distribution of drop sizes," *Int. J. Heat Mass Transfer*, vol. 16, no. 2, pp. 411–425, 1973. DOI: 10.1016/0017-9310(73)90068-9.
[20] P. Li, X. Fan, and Z. Chen, "Numerical study on the heat transfer of micro elliptic pin fins in a rectangular minichannel," *Num. Heat Transfer, Part A: Appl.*, vol. 70, no. 11, pp. 1242–1252, 2016. DOI: 10.1080/10407782.2016.1230430.
[21] D. Ansari, and K. Kim, "Hotspot management using a hybrid heat sink with stepped pin-fins," *Num. Heat Transfer, Part A: Appl.*, vol. 75, no. 6, pp. 359–380, 2019. DOI: 10.1080/10407782.2019.1599272.
[22] J. Zhang, W. Li, and W. J. Minkowycz, "Numerical simulation of R410A condensation in horizontal micro-fin tubes," *Num. Heat Transfer, Part A: Appl.*, vol. 71, no. 4, pp. 361–376, 2017. DOI: 10.1080/10407782.2016.1243934.
[23] H. J. Brusscher, A. W. J. Van Pelt, P. De Boer, H. P. De Jong, and J. Arends, "The effect of surface roughening of polymers on measured contact angles of liquids," *Colloids Surf.*, vol. 9, no. 4, pp. 319–331, 1984. DOI: 10.1016/0166-6622(84)80175-4.
[24] H. Cho, D. Preston, Y. Zhu, and E. Wang, "Nanoengineered materials for liquid–vapor regime-change heat transfer," *Nat. Rev. Mater.*, vol. 2, pp. 16092–1-17, 2016.
[25] M. Kaviany, "Boundary-layer treatment of film condensation in the presence of a solid matrix," *Int. J. Heat Mass Transfer*, vol. 29, no. 6, pp. 951–954, 1986. DOI: 10.1016/0017-9310(86)90191-2.
[26] D. M. Anderson *et al.*, "Using amphiphilic nanostructures to enable long-range ensemble coalescence and surface rejuvenation in dropwise condensation," *ACS Nano*, vol. 6, no. 4, pp. 3262–3268, 2012. DOI: 10.1021/nn300183d.
[27] S. Stylianou, and J. W. Rose, "Dropwise condensation on surfaces having different thermal conductivities," *J. Heat Transfer*, vol. 102, no. 3, pp. 477–482, 1980. DOI: 10.1115/1.3244326.

Appendix A: Experiment and results

The experiments have been described in [10] and here we augment them with large-particle results. The experimentally sintered copper particle monolayer wick on copper substrates was coated with a thiol-based self-assembled monolayer coating. This is to create a hydrophobic copper surface (wick and substrate) to promote dropwise condensation of steam in a custom condensation chamber. The surface is vertically oriented, the average copper particle diameter used ranged from 4 to 416 μm, and the steam pressure (no non-condensable gas) is maintained between 222 and 245 kPa (saturation temperature 378 K to 383 K). The copper particles (ACuPowder) are adhered to the surface with application of a thin layer of Nicrobraz (Wall Colmonoy), and then the test block is sintered to 1,248 K in a hydrogen furnace. The self-assembled monolayer was created using a 5 mM solution of 1 H,1H,2H,2H-perfluorodecanethiol (Sigma-Aldrich) dissolved in 2-propanol (Sigma-Aldrich, St. Louis, MO). The test block is submerged in a sealed bath of the self-assembled coating solution for 24 h and is subsequently dried with dry nitrogen gas.

The measured specific resistance (inverse of the heat transfer coefficient), including error bars, are presented in Figure A.1(a) for the seven average particle diameters and for the plain surface. The results are also listed in Table A.1. Figure A.1(b) shows the snapshots of condensation of all eight surfaces. The tabulated data are listed in the Appendix. The results for the smooth (plain) hydrophobic copper surface is $h_{ps} = 156 \pm 3$ kW/m-K which is in the range of previously reported results [1]. The results show modest improvement of the convective heat transfer coefficient for the smallest particle diameter used in our experiments. Otherwise, the presence of the monolayer wick results in the degradation of thermal performance.

The results suggest a transition where the liquid condensing within the wick structure does not collect in the droplets above the wick, but transports as a film within the wick [26,27]. The results indicate that this transition to decreased thermal performance is most evident for the largest powder diameters (240 and 416 μm, in our new data [16]). For these samples, the increased film thickness beneath the wick structure results in lower performance. The large diameter copper powder particles are too widely spaced to generate small departing droplets with low hysteresis, which prevents the consistent formation of droplets. The droplets experience high hysteresis while thin films form on and within the wick. The theoretical explanation of this data is provided in the following sections.

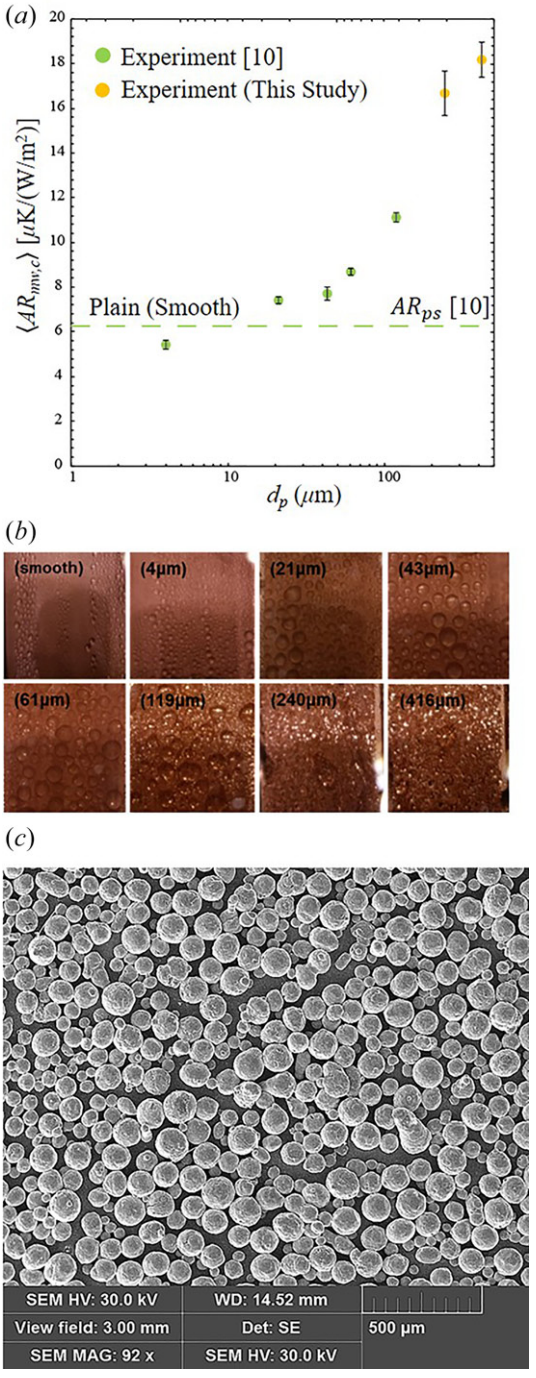

Figure A.1 (*a*) Variations of the measured specific resistance (inverse of the heat transfer coefficient), with the particle diameter (d_p). The results for the plain surface (particle diameter of zero) is also shown. (*b*) Photographic images showing the surface droplets for all eight surfaces. (*c*) Scanning electron microscope (SEM) micrograph of the monolayer.

Table A1. Results of dropwise condensation heat transfer coefficient ($1/\langle R_{mw,c}\rangle$) on plain and monolayer wick coated vertical plate. The results for $d_p = 240$ and 416 μm are from this study, while the rest are from [10].

d_p (μm)	$1/\langle AR_{mw,c}\rangle$ (kW/m^2-K)	Standard Error (±) (kW/m^2-K)
Smooth (Plain)	156	3.3
4	183	6.5
21	134	2.5
43	129	5.0
61	115	1.9
119	97	1.7
240	58	3.4
416	55	2.4